



MATS63330 PGT Dissertation 2020-21

Effect of prior deformation on slip activity in Nickel alloys

Student: Edgar Vivek Mendonca

University ID: 10723573

Supervisor: Dr João Quinta da Fonseca

Guide: Dongchen Hu (PhD)

Department of Materials in the School of Natural Sciences

The University of Manchester

Contents

1	ABSTRACT.....	5
2	INTRODUCTION.....	5
2.1	Aims and Objectives.....	6
3	LITERATURE REVIEW	7
3.1	Exposition of Nickel-625	7
3.2	Phase diagrams and crystal structure.....	8
3.3	Crystal plasticity and Slip activity.....	9
3.4	Relative Displacement Ratio (RDR) analysis	11
3.5	Characterisation techniques	12
3.5.1	Metallography tests	12
3.5.2	Mechanical tests	13
3.5.3	Scanning electron microscopy (SEM) and Electron backscatter diffraction (EBSD)	16
3.5.4	High-Resolution Digital Image Correlation (HRDIC).....	17
4	METHODS.....	18
4.1	Mechanical tests and initial pre-straining.....	18
4.2	Analysis using DefDAP.....	20
4.2.1	High-resolution digital image correlation	20
4.2.2	Electron backscatter diffraction.....	21
4.2.3	Linking HRDIC and EBSD maps	23
4.2.4	RDR analysis of grains	23
5	RESULTS AND DISCUSSIONS.....	25
5.1	Initial HRDIC and EBSD analysis	25
5.2	Measurement of slip activity and RDR analysis	27
5.3	Slip variability within a grain	28
6	CONCLUSIONS.....	29
7	ACKNOWLEDGEMENTS	30
8	REFERENCES	30

List of figures

Figure 1 Improvement of the operating temperature limit of alloys for aircraft turbine engines ³	5
Figure 2 GEnx-1B Boeing 787 engine key characteristics ⁴	6
Figure 3 Characteristic wear types (a) and selection of cutting tool materials (b) in the machining of heat resistant super alloys (HRSA) materials ⁵	6
Figure 4 Micrograph of as-received (annealed) sample of Ni-625 obtained via VIM and ESR process ⁹	8
Figure 5 Ni-Al-Ti ternary phase diagrams show the γ and γ' phase-field ¹⁴	8
Figure 6 Crystal structure of (a) γ phase (b) γ' phase ^{14 13}	9
Figure 7 Lattice vectors along $\langle 110 \rangle$ directions in γ and γ' , lying on $\{111\}$ planes. (a) γ has a random distribution of Ni, Al and Ti atoms (b) γ' has its nickel atoms located at the face-centres ^{14 13}	9
Figure 8 Illustration of slip plane and slip direction (image courtesy of DoITPoMS).....	10
Figure 9 Idealized slip band after half-cycle deformation (a) Geometric parameters of the slip plane and slip direction— α , β , δ , (b) geometric dimensions of the slip step (c) surface displacement and thickness of the slip band ¹⁶	10
Figure 10 Dislocation structure (a) Before and (b) after the half-cycle deformation in tension	11
Figure 11 Schematic representation of RDR analysis via a comparison between the values obtained by using experimental measurement ¹⁸	12
Figure 12 Representation of RDR process for experimental measurement ¹⁹	12
Figure 13 Microstructural features of RR1000 ²⁰	13
Figure 14 INSTRON universal testing machine ²⁶	14
Figure 15 Standard rectangular tensile test specimen (Dog-bone shape) ²⁵	14
Figure 16 Ideal Engineering and True Stress-Strain Curves for a Tensile Test ²⁵	15
Figure 17 Illustration of smaller samples cut from a large pre-strained sample	15
Figure 18 Layout of Scanning electron microscope	16
Figure 19 EBSD results for samples fabricated using high-power CO ₂ laser (a) Inverse pole figure (IPF) (b) 001 and 111 pole figure ²⁹	17
Figure 20 Representation of strain field mapping using Digital Image correlation ³¹	17
Figure 21 HRDIC strain map produced for tension and reversal of load with grain boundaries represented using white boundaries ²⁸	18
Figure 22 Dimensions of the large dog-bone tensile test sample (image courtesy of Dongchen Hu) .	19
Figure 23 Quasi-static tensile test conducted on a universal testing machine	19
Figure 24 Stress-Strain curve obtained from pre-straining large Nickel sample	20
Figure 25 Maximum shear stress using HRDIC	20
Figure 26 EBSD maps obtained from analysis (A) Euler Map (B) IPF Map (C) Kam Map (D) Average Grain Schmid Factors Map	21
Figure 27 IPF Maps for directions (A) [1,0,0] (B) [0,1,0] (C) [0,0,1] directions	22
Figure 28 IPF colour key ³³	22
Figure 29 Single grain analysis (A) spread of orientation on an IPF Map (B) Unit Cell (C) GROD	22
Figure 30 Multi grain analysis (A) All grain orientation in IPF map (B) GROD for the entire map	23
Figure 31 Transformation map obtained via linking HRDIC and EBSD maps.....	23
Figure 32 Grain selected for RDR analysis (e.g.: Grain ID 29)	24
Figure 33 RDR analysis conducted on a single grain (A) selection of slip band for analysis (B) u versus v centred values as the gradient of the linear regression	24
Figure 34 HRDIC map obtained for Ni alloys analysis	25
Figure 35 EBSD maps for Ni based superalloys analysis (A) Euler Map (B) IPF Map (C) Kam Map (D) Average Grain Schmid Factors Map.....	25

Figure 36 Single grain analysis (A) spread of orientation on an IPF Map (B) Unit Cell (C) GROD, obtained for Grain ID 542	26
Figure 37 Multigrain analysis (A) Grain orientation in IPF map (B) GROD, obtained for the entire map	27
Figure 38 Grain selected for further analysis (Grain ID: 7)	28
Figure 39 Selection of slip bands to identify variability within a grain	29
Figure 40 Dimensions of test sample for in-situ test	30

List of tables

Table 1 Composition detail of Ni-625 (Inconel-625) ⁸	7
Table 2 Properties of Ni-625 ⁸	7
Table 3 Composition of Inconel-625 alloy obtained by vacuum induction melting (VIM) and electro slag refining/remelting (ESR) processes ⁹	8
Table 4 Homologous points for DIC and EBSD maps	27
Table 5 Results from RDR calculation for the selected grains	28
Table 6 Results obtained for slip variability within a grain (for grain ID: 7)	29

List of equations

1	10
2	14
3	14
2	18

1 ABSTRACT

The impact of slip occurrence in materials determines the large displacement of a crystal structure. In a study conducted on nickel superalloys, the slip activity is measured on initially pre-strained specimens in different directions. The incidence of slip, crystal/grain orientation and microstructure can be analysed by obtaining high-resolution digital image correlation (HRDIC) and EBSD maps. The effect of change in slip paths in different directions of loading is studied in order to quantify which slip system is likely to be active and cause the failure of the specimen. The HRDIC data quantifies slip bands within single grains and the EBSD data quantifies lattice rotations associated with the slip activity due to microstructural constraint. The analysis revealed the slip activity in every grain of the deformed specimen and conjunction with relative displacement ratio (RDR) analysis, the active slip systems can be identified and compared with theoretical analysis obtained via Schmid factor calculations.

2 INTRODUCTION

Superalloys are high-performance materials widely used in aerospace and energy industries as key structural materials. Superalloys can be a group of nickel, iron-nickel and cobalt-based alloys. They are classified as alloys based on group VIIIA-base elements used in components that demonstrate reliable mechanical properties at extreme service temperatures.^{1 2}

Figure 1 demonstrates an improvement in creep resistance using for jet engines, an industry benchmark of maximum temperature that materials can withstand without failing when loaded.

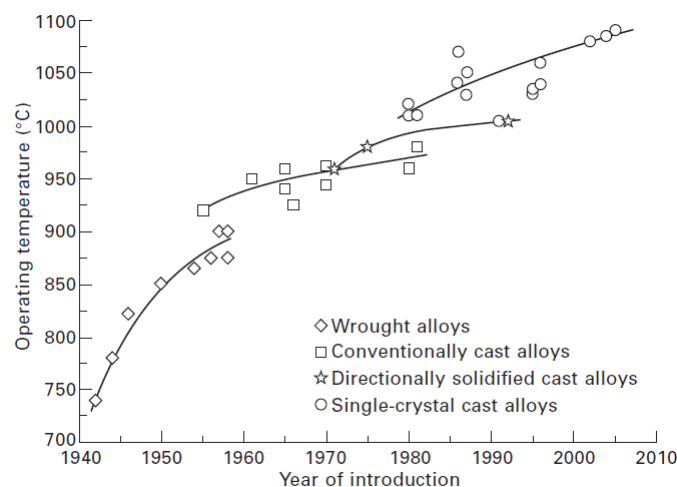


Figure 1 Improvement of the operating temperature limit of alloys for aircraft turbine engines³

Superalloys such as nickel-based find application in jet engines where high-performance at extremely high operating temperature becomes vital. The classification of materials used in a modern jet engine is represented in Figure 2. Superalloys account for 50% of the total weight of the material in such components. Nickel-based superalloys find application in components such as turbine blades, discs, vanes, and combustion chambers where the in-service temperature reaches up to 1900°C.

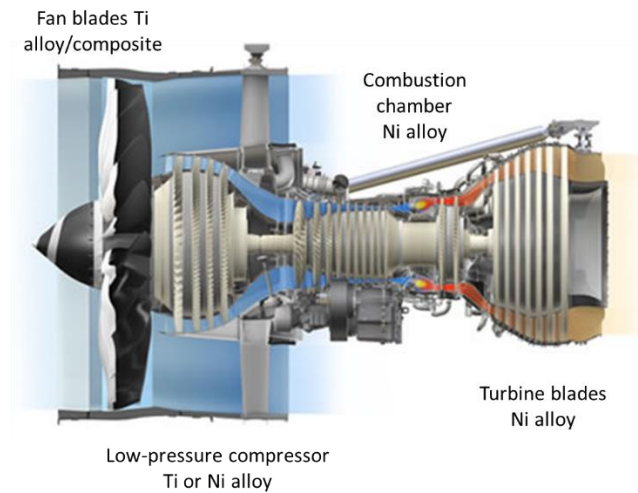


Figure 2 GEnx-1B Boeing 787 engine key characteristics ⁴

Machinability is one of the keys aspects of material property and is termed as the ease with which a material can be machined to the desired shape using the appropriate cutting tool. Nickel-based superalloys are generally classified as harder to machine, pertaining to their high strength, hardness even at high temperatures. Hence the use of hybrid machining processes, such as thermal-assisted machining, cryogenically enhanced machining, and media-assisted machining, are favoured. Figure 3a describes the wear characteristic for different nickel alloys selection of cutting tool based on hardness, heat treatment. Based on these characteristics, an appropriate tool (Figure 3b) for different machining speeds and feed rates ⁵.

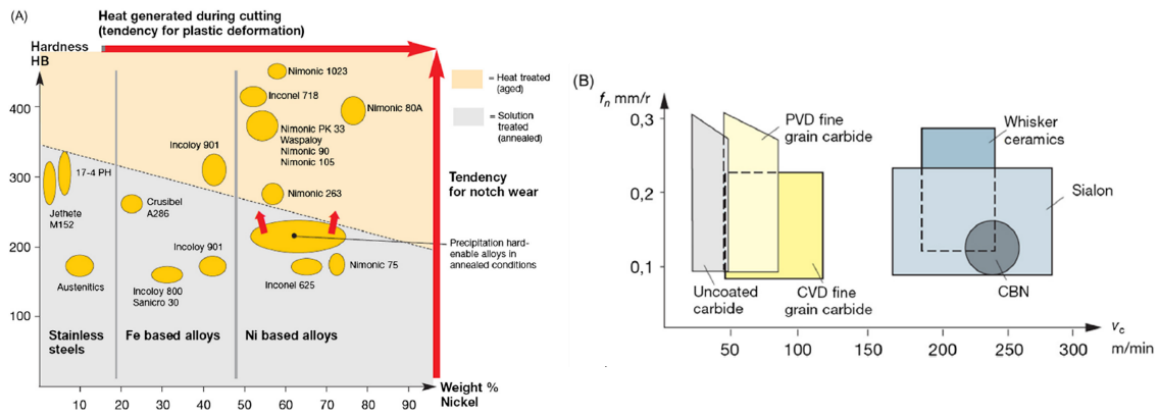


Figure 3 Characteristic wear types (a) and selection of cutting tool materials (b) in the machining of heat resistant super alloys (HRSA) materials ⁵

2.1 Aims and Objectives.

The key aims of this research are to quantify the effects of the previously loaded and deformed sample and to study the slip activity during reloading along different strain paths. The material selected for the research is Nickel/Inconel 625. The technique of High-resolution digital image correlation (HRDIC) combined with electron backscatter diffraction (EBSD) can be combined to understand the slip band

interactions ⁶. The smaller samples are machined from the large, preloaded specimen by electric discharge machining (EDM) to geometry ⁷. The main objectives of this research include:

- To preload, a large sheet of known thickness, so that smaller samples can be extracted from at the same at 0,45 and 90 degrees.
- The mechanical properties must be determined when reloading.
- The grain orientation is determined using EBSD.
- Slip activity is measured using high-resolution digital image correlation (HRDIC).
- To relate the slip activity in the pre-strained tensile test sample of nickel measured at different directions using high-resolution digital image correlation.

3 LITERATURE REVIEW

3.1 Exposition of Nickel-625

A brief description of Inconel-625 (Nickel-based superalloy) is provided regarding its composition, physical, mechanical properties and corresponding microstructure based on different heat treatment processes. Ni-625 series of Nickel has chromium as its primary alloying element. Table 1 gives the composition of Nickel-chromium alloy, INCONEL 625, in the annealed state and Table 2 represents the physical and mechanical properties. The details were obtained from ANSYS Granta EduPack ⁸.

Table 1 Composition detail of Ni-625 (Inconel-625) ⁸

Element	Composition %
Al (aluminium)	0-0.4
C (carbon)	0-0.1
Co (cobalt)	0-1
Cr (chromium)	20-23
Fe (iron)	0-5
Mn (manganese)	0-0.5
Mo (molybdenum)	8-10
Nb (niobium)	3-4.15
Ni (nickel)	58-66
P (phosphorus)	0-0.015
S (sulphur)	0-0.015
Si (silicon)	0-0.5
Ta (tantalum)	0-0.15
Ti (titanium)	0-0.4

Table 2 Properties of Ni-625 ⁸

Property	Unit	Value
Density	kg/m ³	8.4e3 - 8.48e3
Young's modulus	GPa	205 - 216
Yield strength (elastic limit)	MPa	365 - 434
Tensile strength	MPa	814 - 900
Poisson's ratio	-	0.28 - 0.291
Hardness - Vickers	VHN	145 - 250
Melting point	°C	1.29e3-1.35e3
Fracture toughness	MPa.m ^{0.5}	190-211
Toughness	kJ/m ²	171-212

Sukumaran et. al. describes a process of obtaining Ni-625 alloys via vacuum induction melting and electro slag refining ^{9 10}. The composition of alloys obtained through this process is given in Table 3 and the corresponding microstructure is represented in Figure 4.

Table 3 Composition of Inconel-625 alloy obtained by vacuum induction melting (VIM) and electro slag refining/remelting (ESR) processes ⁹

Elements	Cr	Mo	Fe	Nb	Co	Ti	Al	C	Mn	Si	S	P	Ni
wt.%	20.9	9	0.93	4	0.01	0.2	0.18	0.08	0.02	0.08	0.01	0.01	Bal

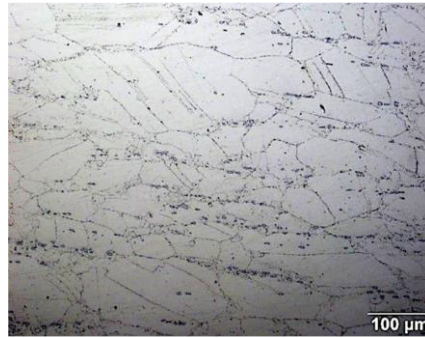


Figure 4 Micrograph of as-received (annealed) sample of Ni-625 obtained via VIM and ESR process ⁹

3.2 Phase diagrams and crystal structure

The existence of phases in the material that has more than one component is determined by phase diagrams ¹¹. The solutes in Ni-based superalloys are Al and Ti with concentrations less than 10 atomic%. This leads to the generation of a two-phase equilibria microstructure, and this comprises γ and γ' ^{12 13}.

γ' precipitates are responsible for providing strength at an elevated temperature that is also responsible to provide resistance to creep deformation. The amount of γ' relies on the composition and service temperature and this is illustrated in the ternary phase diagrams for Ni-Al-Ti in Figure 5.

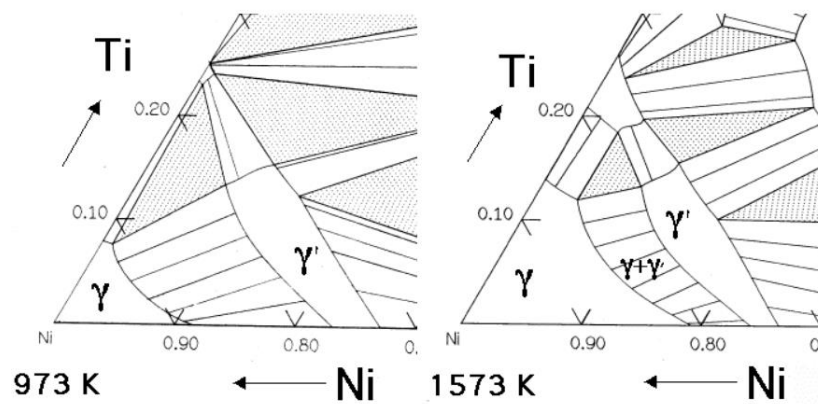


Figure 5 Ni-Al-Ti ternary phase diagrams show the γ and γ' phase-field ¹⁴

The γ -phase is a solid solution with face centred cubic lattice with randomly distributed atoms (Figure 6a). For γ' the lattice structure is a primitive cell (as the central atom is different) where the Al and Ti atoms occupy the corners and Ni occupies the face centres (Figure 6b). The γ' precipitates lead to the formation of the γ phase. The γ' precipitates lead to the formation of the γ phase.

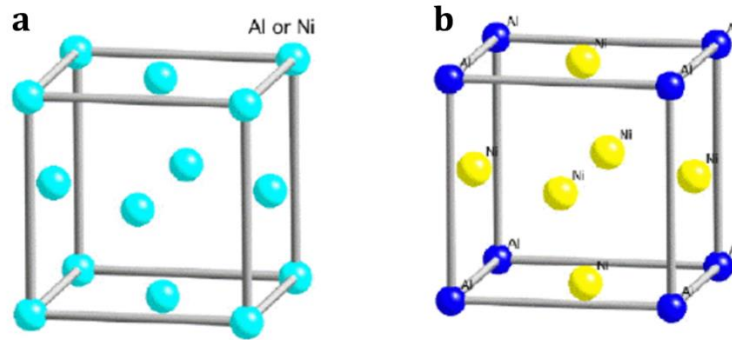


Figure 6 Crystal structure of (a) γ phase (b) γ' phase ^{14 13}

The presence of the γ' phase impedes the motion of dislocations as it has an ordered crystal structure. For γ , the Burgers vector of dislocation is $\frac{a}{2} \langle 110 \rangle$, so that the lattice vector does not slip and alter the crystal structure (Figure 7a). However, for γ' the lattice vector $\frac{a}{2} \langle 110 \rangle$ is given for a primitive cubic lattice as the atom at the face centre is different (Figure 7b).

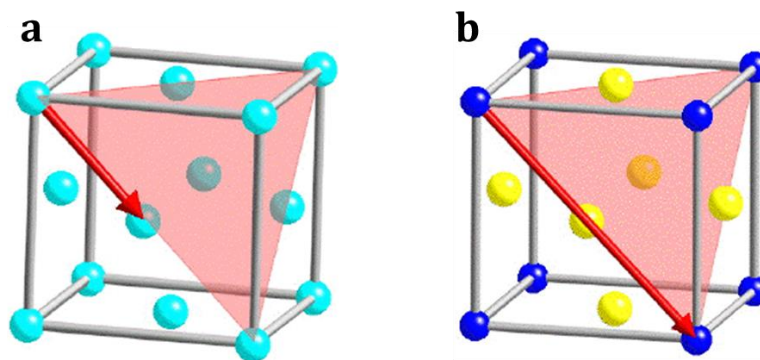


Figure 7 Lattice vectors along $\langle 110 \rangle$ directions in γ and γ' , lying on $\{111\}$ planes. (a) γ has a random distribution of Ni, Al and Ti atoms (b) γ' has its nickel atoms located at the face-centres ^{14 13}

3.3 Crystal plasticity and Slip activity

Slip occurs due to the motion of dislocations. This is initiated by the amount of stress applied, as illustrated in Figure 8. Slip occurs only when shear stress acting in the slip direction on the slip plane reaches a critical value. This initiation of the slip in grains is given as a component of shear stress known as critical resolved shear stress and the component of shear stress is known as resolved shear stress. Slip occurs only when resolved shear stress value is greater than critical resolved shear stress.

Slip planes and the slip directions are given by the Schmid factor ¹⁵. Slip primarily occurs on grains with the highest Schmid factor value. The resolved shear stress on the slip plane parallel to the slip direction is given as,

$$\tau_R = \frac{F \cos \lambda}{A / \cos \psi} = \frac{F}{A} \cos \psi \cos \lambda \quad 1$$

The value of τ_R at which slip occurs is a constant, known as the critical resolved shear stress τ_c . This is defined as Schmid's Law.

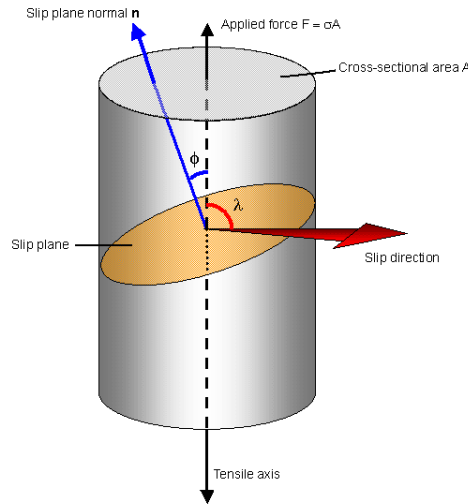


Figure 8 Illustration of slip plane and slip direction (image courtesy of DoITPoMS)

For polycrystalline materials, the deformation mechanism is governed by slip bands formed under loading. Slip contributes to grain orientation. There are one or more slip systems with each grain boundary that results in a single-dominant of parallel slip bands across the grain ^{16 17}.

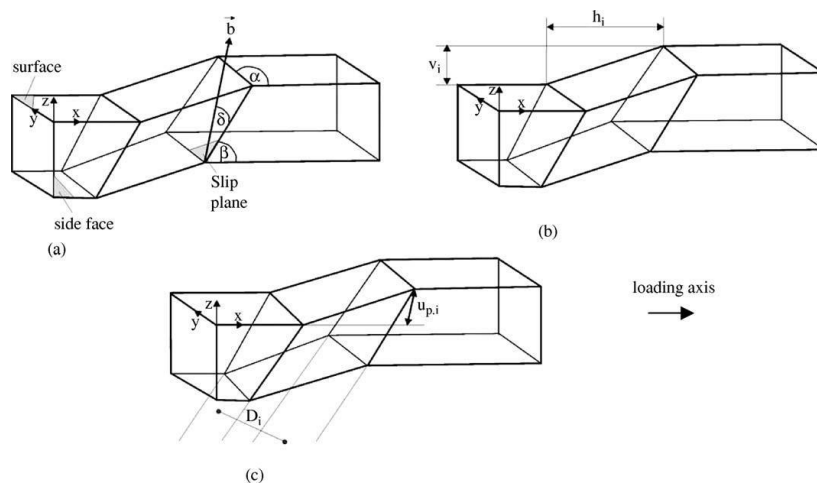


Figure 9 Idealized slip band after half-cycle deformation (a) Geometric parameters of the slip plane and slip direction— α , β , δ , (b) geometric dimensions of the slip step (c) surface displacement and thickness of the slip band ¹⁶

Figure 9 gives the appearance of slip bands after a half-cycle deformation in tension. The geometric parameters calculated from EBSD-orientation is illustrated in Figure 9a. α is the angle between the trace of the slip plane in the x-direction (loading axis) on the surface. β and δ are the angles between the trace of the slip plane on the side face and the x-axis and the Burgers vector. Persistent slip bands formed after half cycle deformation is represented in Figure 10 and the newly formed steps are visible as dark thin lines.

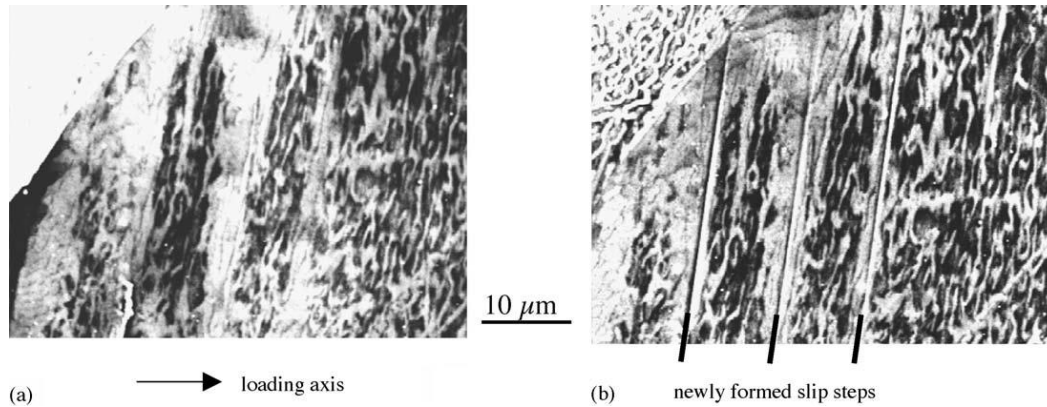


Figure 10 Dislocation structure (a) Before and (b) after the half-cycle deformation in tension

3.4 Relative Displacement Ratio (RDR) analysis

RDR analysis is based on possible Burgers vectors in association with displacement gradient across the slip trace. This can be used to determine using the crystallographic information from EBSD and the displacement maps from HRDIC. In Figure 11, an illustration of measurement of experimental RDR value from HRDIC displacement map is indicated and the value is the ratio of the relative displacements along with the x and y directions from one side of the slip band to the other. The ratio is calculated from multiple measurements conducted along with the slip band as the slope of a line fitted using a linear regression^{18 19}.

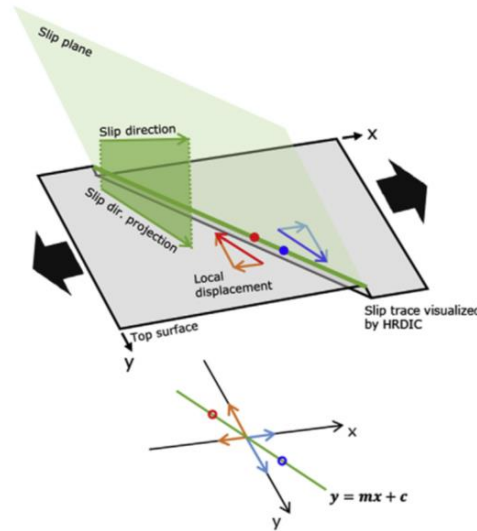


Figure 11 Schematic representation of RDR analysis via a comparison between the values obtained by using experimental measurement ¹⁸

Figure 12 demonstrates the RDR process obtained from EBSD and the displacement maps from HRDIC. The first figure (a-1) slip trace from an HRDIC strain map. The figures (a-2) and (a-3) are changes in the displacements from one side of the slip trace to the other indicated as u-displacement and v-displacement respectively. A scatter plot of u/s v centred values of a linear regression gives the experimental RDR value (a-4).

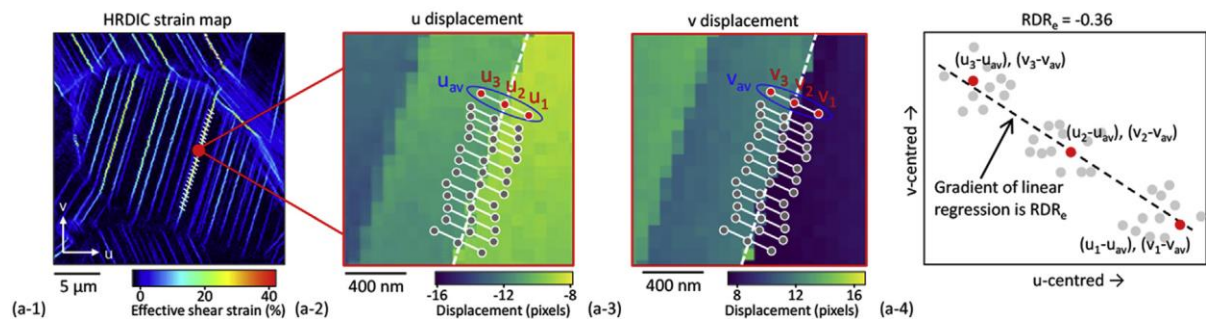


Figure 12 Representation of RDR process for experimental measurement ¹⁹

3.5 Characterisation techniques

3.5.1 Metallography tests

The study of the physical structure and components of a metal or an alloy using is a microscope is termed microscopy. A study on polycrystalline nickel alloy RR1000 conducted by Whittaker et. al., reveals primary ($\sim 5 \mu\text{m}$ diameter) and secondary γ' ($\sim 0.2 \mu\text{m}$ diameter) precipitates as in Figure 13.

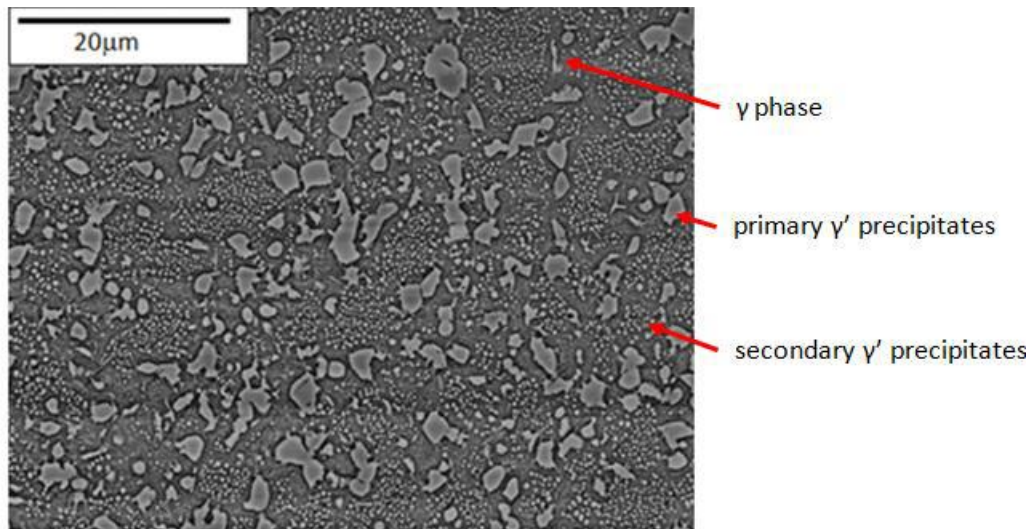


Figure 13 Microstructural features of RR1000 ²⁰

In this research, an inspection of the metallography of Inconel-625 will be conducted to reveal its microstructural features. The specimen to be examined must be cut to a suitable size. The cut specimens are then subjected to grinding may be performed manually or on power-driven wheels using silicon carbide paper disks. The indents and the scratch from the grinding process are removed by polishing ^{21 22}.

3.5.2 Mechanical tests

A tensile test is the most common experimental technique used to determine the mechanical properties of a material. Properties of materials such as Young's Modulus, Poisson's ratio, hardness, yield strength, tensile strength, toughness, ductility, creep characteristics, fatigue behaviour, fracture toughness are essential in design, structural applications ²³.

These properties of materials are determined from tensile tests conducted on a universal testing machine (Figure 14) on standard dog-bone shaped test samples (Figure 15). The dog bone shaped specimen is preferred as promotes failure within the gauge length as the mechanical and physical measurements are done within the gauge length of the test sample with the help of an extensometer. The methods for conducting a tensile test, preparation of specimens and measurements are standardised by standardization organizations such as ISO and ASTM ^{24 25}.

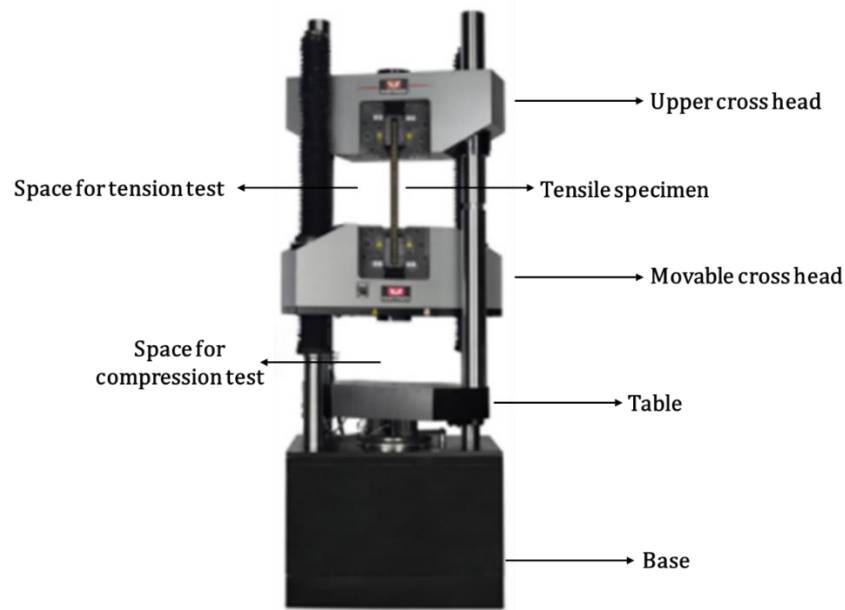


Figure 14 INSTRON universal testing machine ²⁶

The ISO standard suggests a relation between the gauge length of the specimen and cross-sectional area across the perpendicular, which is given as,

$$L_0 = 5.65\sqrt{A_0} \quad 2$$

And the area of cross-section A_0 of the test specimen, that is given as,

$$A_0 = bt \quad 3$$

Where b and t are the width and the thickness, respectively.

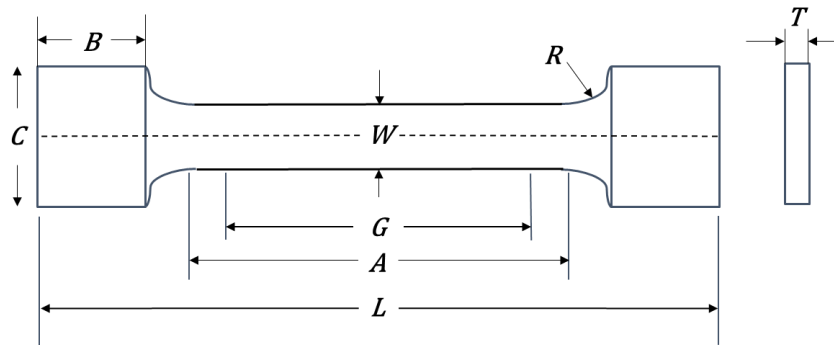


Figure 15 Standard rectangular tensile test specimen (Dog-bone shape) ²⁵

From a tensile test, a load-extension plot is obtained which in turn can be interpreted as a stress-strain plot (Figure 16) which determines the material behaviour under quasi-static loading. The ideal plots for true and engineering stress-strain are for any given material is also illustrated indication of the elastic and the plastic regions. The slope of the elastic region gives Young's Modulus of the material.

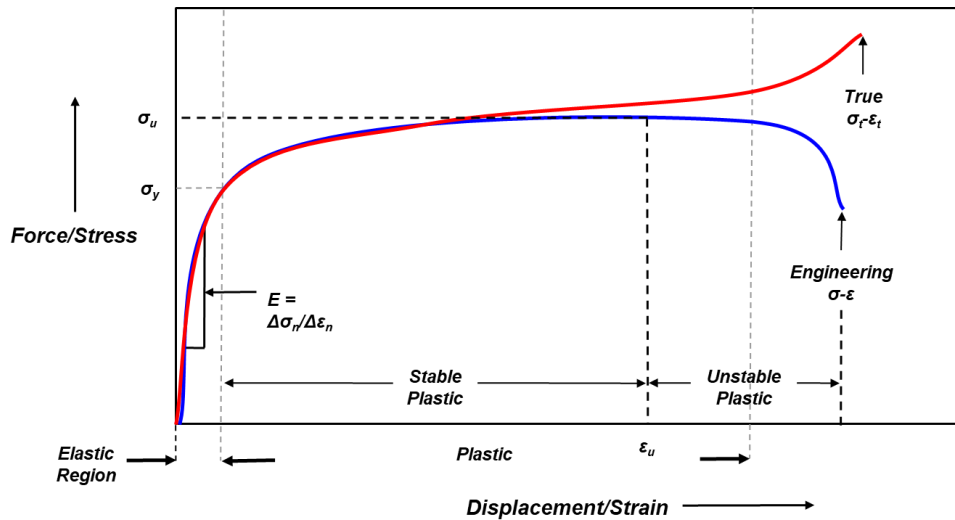


Figure 16 Ideal Engineering and True Stress-Strain Curves for a Tensile Test ²⁵

In this research, initial tensile tests will be conducted on a large specimen of nickel on a universal testing machine to characterise the mechanical properties and pre-strain the sample to a defined strain percentage. In later stages, smaller samples will be extracted from the large pre-strained sample using wire EDM (electric discharge machining) in different directions (0°, 45°, 90°) as illustrated in Figure 17.

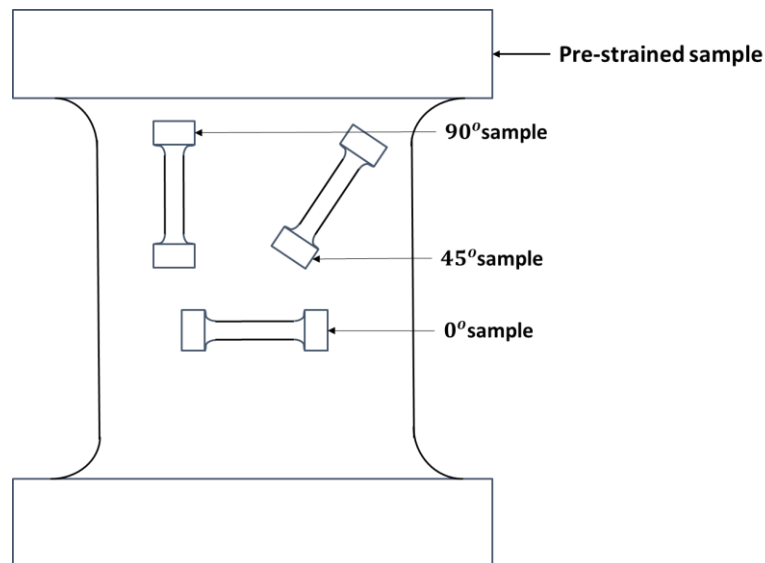


Figure 17 Illustration of smaller samples cut from a large pre-strained sample

3.5.3 Scanning electron microscopy (SEM) and Electron backscatter diffraction (EBSD)

A Scanning Electron Microscope (SEM) is a classification of electron microscope that uses a focused beam to produce a magnified image of the given sample. The electron beam scans the surface of the sample and the electrons that interact produce various signals that contain information about the surface topography and composition.

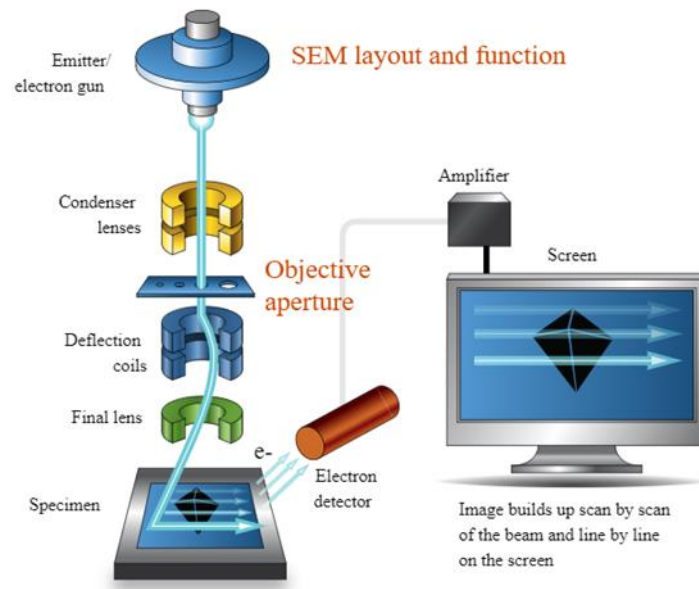


Figure 18 Layout of Scanning electron microscope

SEM uses high energy electrons beam generated by an electron gun and processed by magnetic lenses. The electron beam is focused on the specimen surface and systematically scanned across the surface. Nevertheless, the electrons in SEM never form a real image. The major components of an SEM are the electron gun, vacuum system, water chilling system, column, specimen chamber, detectors and the imaging system that includes acquisition and display (Figure 18) ²⁷.

Electron Backscatter Diffraction (EBSD) is an experimental technique that allows the investigation of crystal orientation of materials for crystalline and polycrystalline materials. The information that can be obtained from this technique is grain size and morphology, texture, and defects. An EBSD detector must be installed on to an SEM. The specimen must be prepared to be flat and smooth so that the topography effects do not interfere with the analysis ^{27 28}.

An EBSD rendering is represented in Figure19 fabricated using a high-power CO₂ laser. The inverse pole figure (Figure 19a) is used to derived crystal orientation from EBSD maps. The orange and red colours in the centre compared to various colours of a random orientation (Figure 19b) indicating well-developed grains axial [001] <110>.

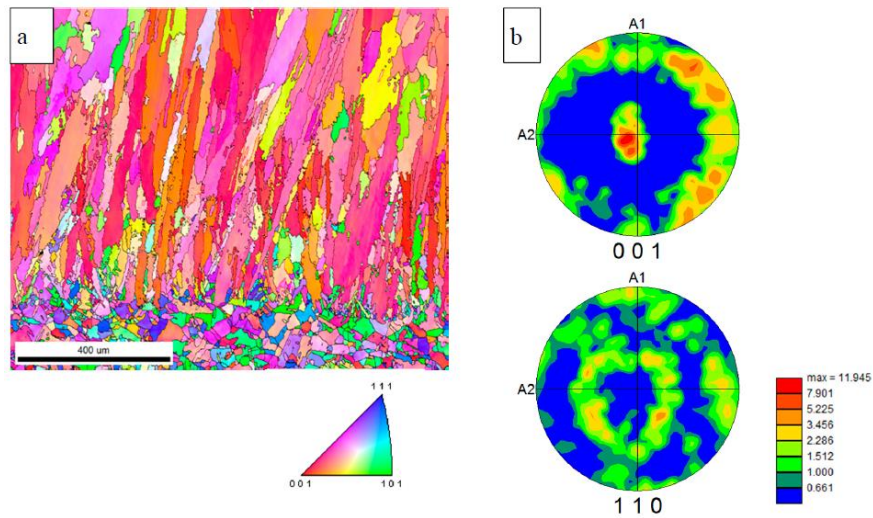


Figure 19 EBSD results for samples fabricated using high-power CO2 laser (a)Inverse pole figure (IPF) (b)001 and 111 pole figure ²⁹

3.5.4 High-Resolution Digital Image Correlation (HRDIC)

Digital image correlation (DIC) is an experimental technique that uses a non-contact optical instrument to measure deformation, vibration, and strain on any material. The technique is combined in conjunction with mechanical testing of materials like tension or compression experiments usually conducted on a universal testing machine. This technique often opts in 2D and 3D measurements of change in images.

DIC utilizes the displacement patterns that are discretised subsets of the whole image taken. A subset is a group of pixels carrying. The maximum correlation in each window corresponds to the displacement, and this gives the vector length and direction for each window (Figure 20) ³⁰.

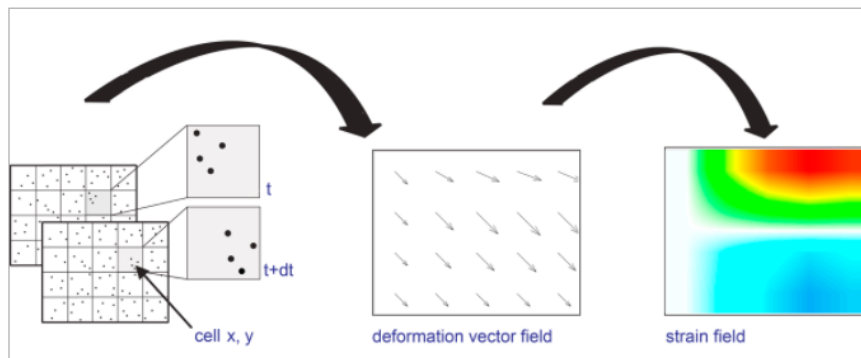


Figure 20 Representation of strain field mapping using Digital Image correlation ³¹

The method of high-resolution digital image correlation (HRDIC) is an imaging technique used to measure local deformation in-situ and over a large area. In HRDIC, the surface strain maps are collected at each deformation step (HRDIC at the four distinct macroscopic strain steps) Figure 30. The effective shear strain, defined as,

$$\varepsilon_{eff} = \sqrt{\left(\frac{\varepsilon_{xx} - \varepsilon_{yy}}{2}\right)^2 + \varepsilon_{xy}^2}$$

Where ε_{xx} is the strain in the loading direction, ε_{yy} is the in-plane transverse strain and ε_{xy} is the in-plane shear strain. The effective shear strain is a measure that assumes that all the deformation has occurred ²⁸.

Estimated transformation obtained from HRDIC and EBSD maps is obtained and represented in Figure 21. The grain boundaries are represented with white borders overlay on the strain map. From the grain boundaries, the shear strain is concentrated along the straight twin boundaries, i.e., the intense slip bands lie along the {111} plane as twin boundary.

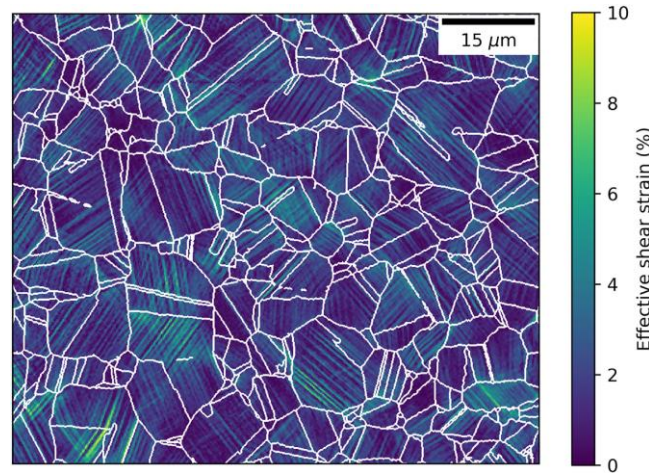


Figure 21 HRDIC strain map produced for tension and reversal of load with grain boundaries represented using white boundaries ²⁸

In this research, the collected EBSD data is derived from the grain boundaries by a critical misorientation. The boundaries are transformed into HRDIC references to map the local strain development and slip activity.

4 METHODS

4.1 Mechanical tests and initial pre-straining

A large tensile sample (dog-bone shaped) will be pre-strained under a universal testing machine to a plastic limit of 10-12% plastic strain. The dimensions of the sample are mentioned in Figure 22. The total length of the machined specimen is 215mm. The functioning of the reference length used in the elongation calculations is referred to as gauge length that determines the initial cross-sectional area before testing the specimen and is 85mm in length. The thickness of the specimen is 2mm. The experiment was conducted on INSTRON universal testing machine (Figure 23). A longitudinal extensometer was used to measure the deformation in the gauge length area during testing.

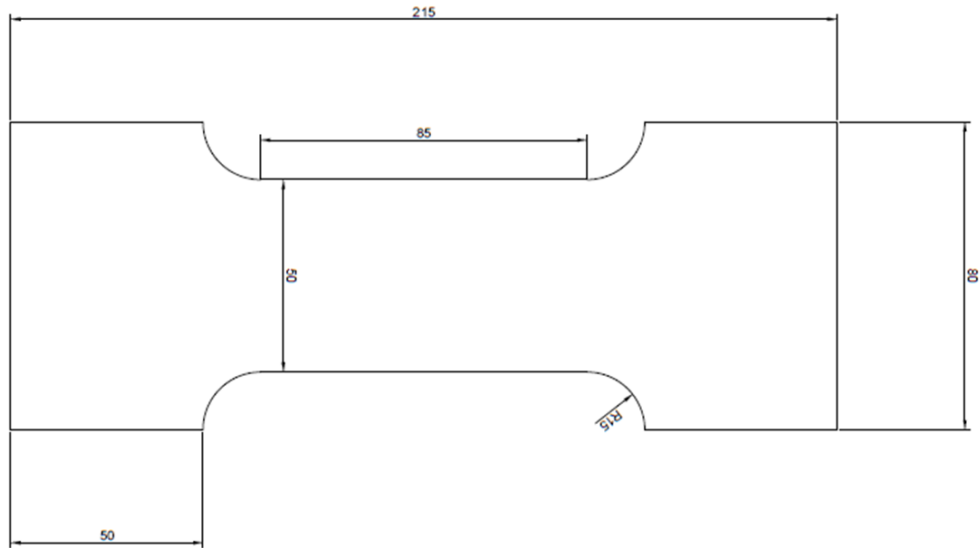


Figure 22 Dimensions of the large dog-bone tensile test sample (image courtesy of Dongchen Hu)

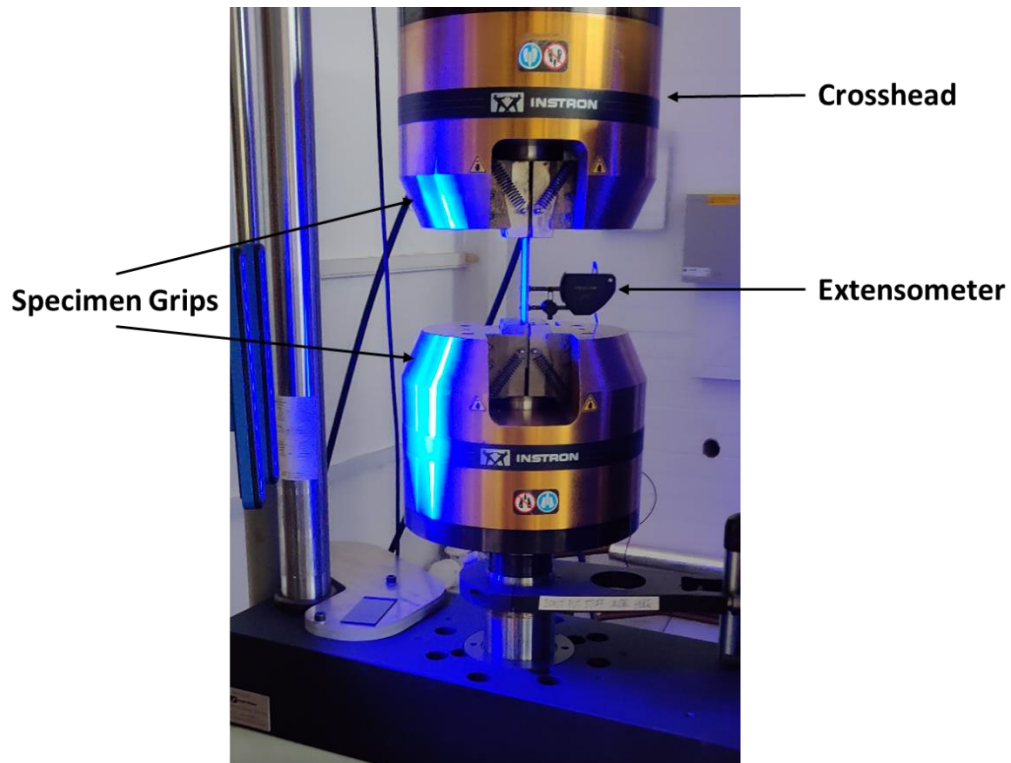


Figure 23 Quasi-static tensile test conducted on a universal testing machine

From the tensile test conducted, the following stress-strain data was obtained as in Figure 24. The sample was deformed up to 12% plastic strain and the yield and ultimate stress obtained are 553.4MPa and 814.7MPa respectively.

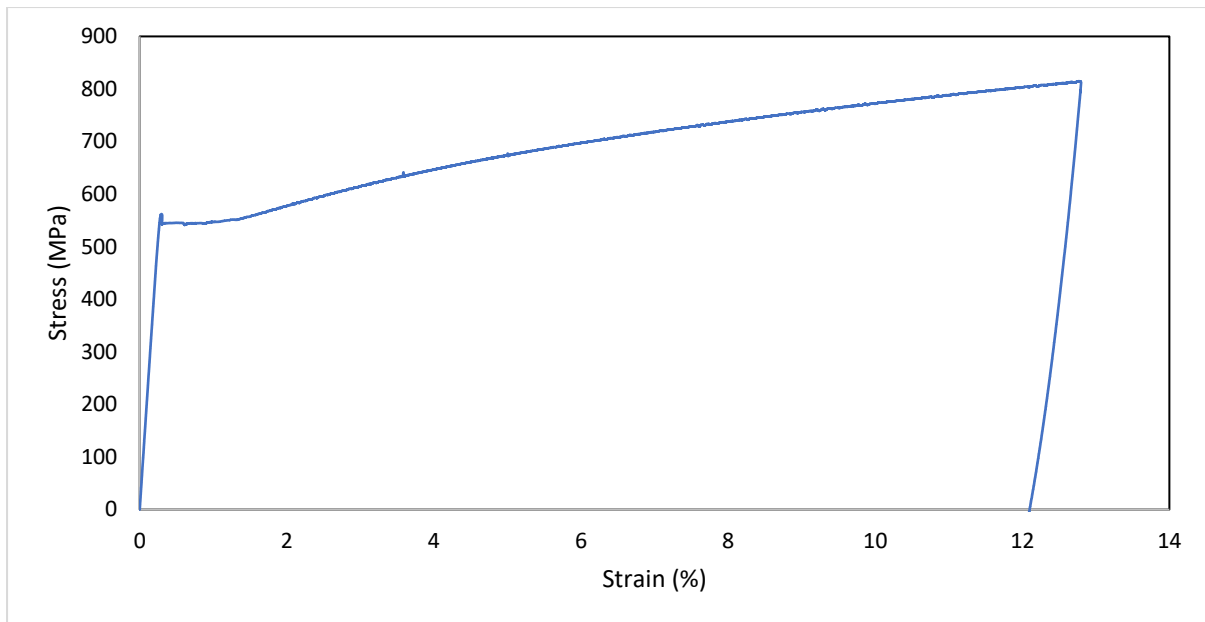


Figure 24 Stress-Strain curve obtained from pre-straining large Nickel sample

4.2 Analysis using DefDAP

Deformation data analysis in python or DefDAP is a python library used for correlating EBSD and HRDIC data ³². Analysis can be conducted to obtain corresponding HRDIC and EBSD results and maps. The following data and results were obtained from conducting analysis for Nickel 625 alloy.

4.2.1 High-resolution digital image correlation

To understand the development of local plastic strain and slip bands, techniques such as high-resolution digital image correlation is utilized. Figure 25 represents the effective shear strain obtained using HRDIC. The scale bar in the figure represents the value of the effective shear strain. In the HRDIC image, the maximum shear strain bands are visible as embodied from the scale bar.

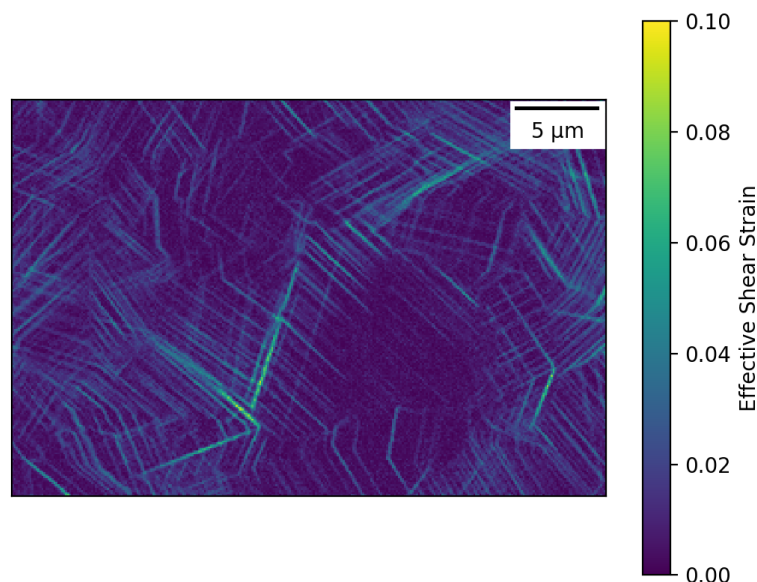


Figure 25 Maximum shear stress using HRDIC

4.2.2 Electron backscatter diffraction

From the EBSD analysis conducted the following results were obtained as depicted in Figure 26. In Figure 26A, the image depicts the Euler map that can be used to determine the crystal orientation matrix and demonstrate the rotation of cartesian vectors used in the generation of microstructure maps.

An IPF map is obtained in the direction $[1,0,0]$ direction in Figure 26B. Similar IPF maps can be obtained in $[0,1,0]$ and $[0,0,1]$ directions (Figure 27). The inverse pole figure map is stereographic projections plotted relative to crystal axes. The selected viewing direction and measured orientation are based on the colour assigned from an IPF colour key (Figure 28).

Measurement of local grain misorientation can be obtained from Kernel average misorientation (KAM) (Figure 26C) during electron backscatter diffraction (EBSD) analysis. The activation of slip in every grain can be estimated using a Schmid factor map. In Figure 26D, the scalebar in the image represents the values of the Schmid factor obtained in the map. The slip in grain is most likely to be activated where the Schmid factor values are high.

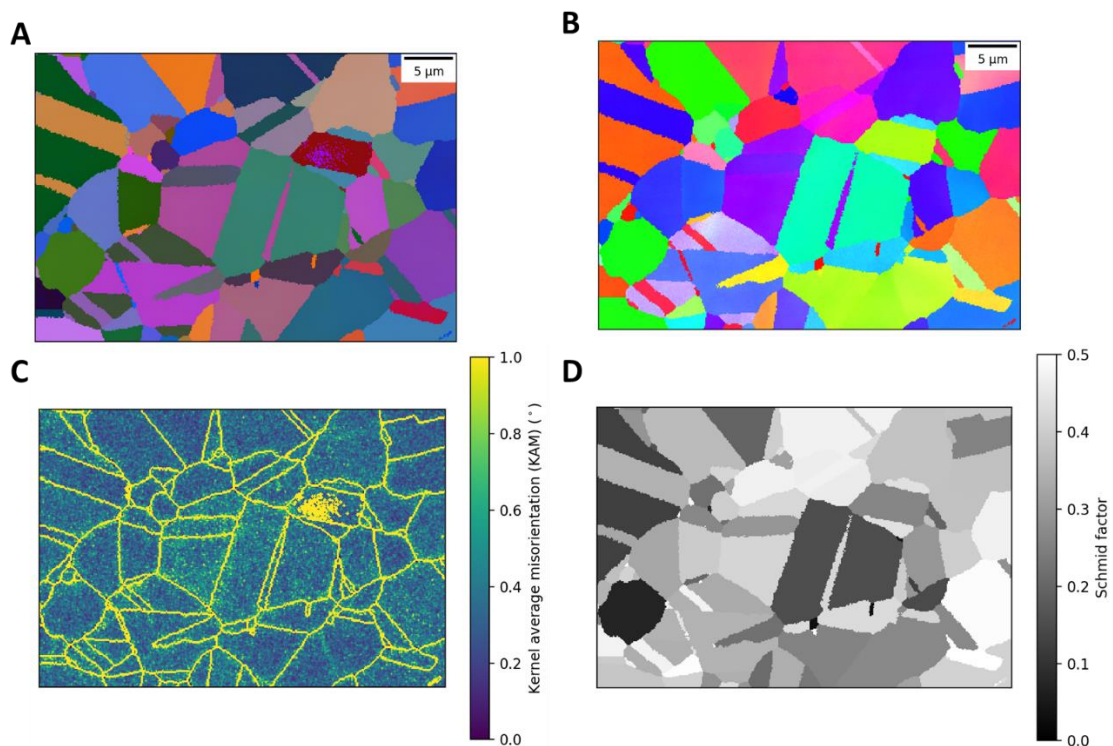


Figure 26 EBSD maps obtained from analysis (A) Euler Map (B) IPF Map (C) Kam Map (D) Average Grain Schmid Factors Map

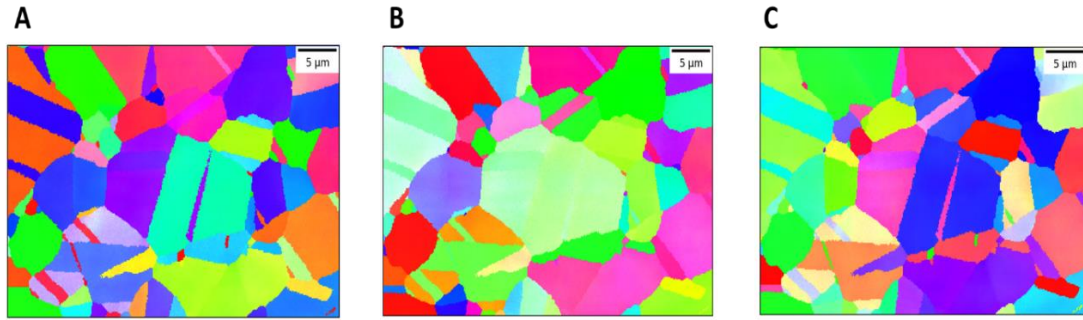


Figure 27 IPF Maps for directions (A) $[1,0,0]$ (B) $[0,1,0]$ (C) $[0,0,1]$ directions

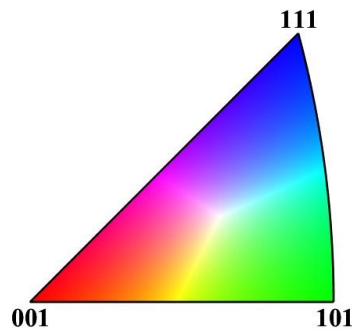


Figure 28 IPF colour key³³

To realize the grain orientation and spread of orientation, a single grain can be selected, and the following analysis can be conducted to obtain the following results (Figure 29). In the following example analysis, Grain ID 50 was selected for further understanding.

For the selected grain, the corresponding spread of orientation is obtained on an IPF map (Figure 29A), and the orientation of the unit cell is represented in Figure 29B. Grain reference orientation deviation maps depict the orientation heterogeneities that develop during deformation (Figure 29C). Every pixel in the grain is established on misorientation of the point relative to a reference orientation and is colour based.

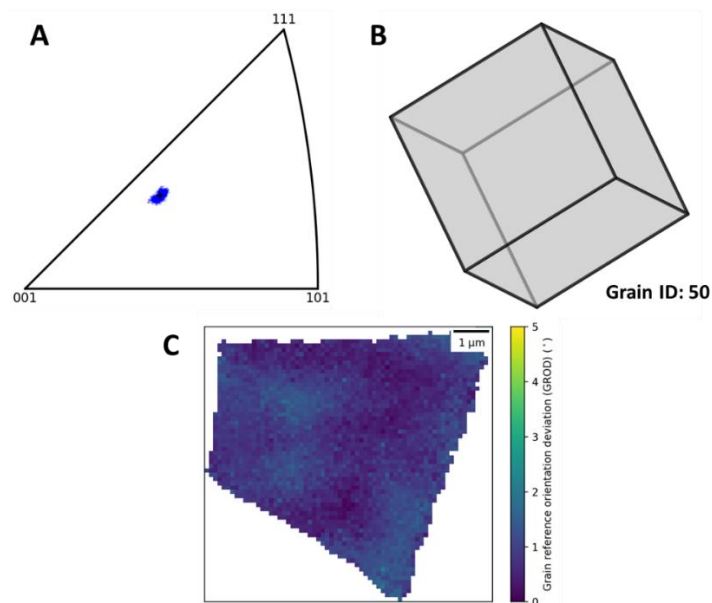


Figure 29 Single grain analysis (A) spread of orientation on an IPF Map (B) Unit Cell (C) GROD

In Figure 30, a multi-grain analysis has been procured. From the analysis for single grain has been obtained, the same can be applied to all the grains in a map using a loop over the grains and the corresponding spread of orientation can be obtained on an IPF map (Figure 30A). Similarly, the GROD for all the grains is obtained (Figure 30B) ³⁴.

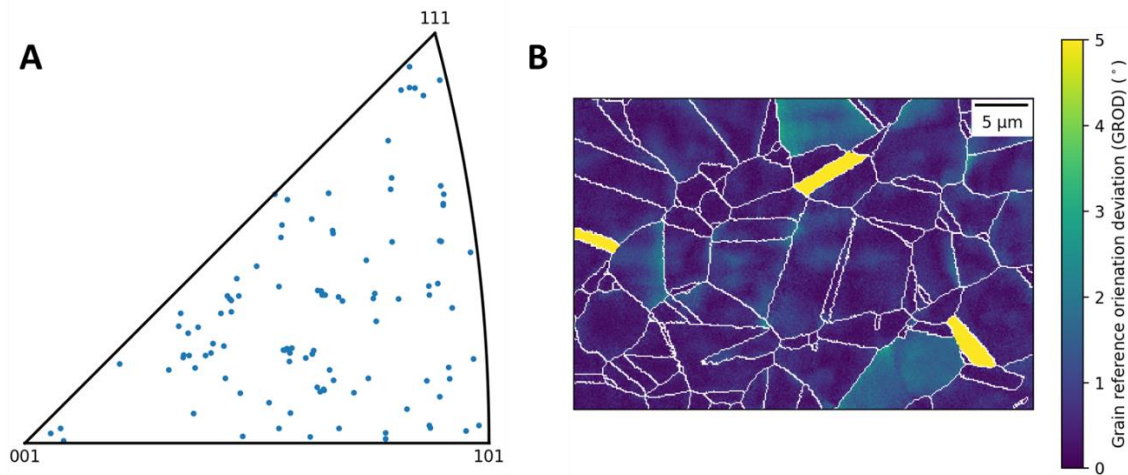


Figure 30 Multi grain analysis (A) All grain orientation in IPF map (B) GROD for the entire map

4.2.3 Linking HRDIC and EBSD maps

4.2.4 RDR analysis of grains

In the further analysis conducted, the HRDIC and EBSD maps are linked. To register the two datasets of HRDIC and EBSD maps, points at the same material location must be defined and is known as homologous points. Transformation is necessary as the EBSD samples are usually tilted at 70° relative to the normal incidence of the electron beam. Hence the transformation map appears to be tilted (as a parallelogram) in Figure 31. The specimen is tilted to optimise the contrast in the diffraction pattern and the electrons scattered.

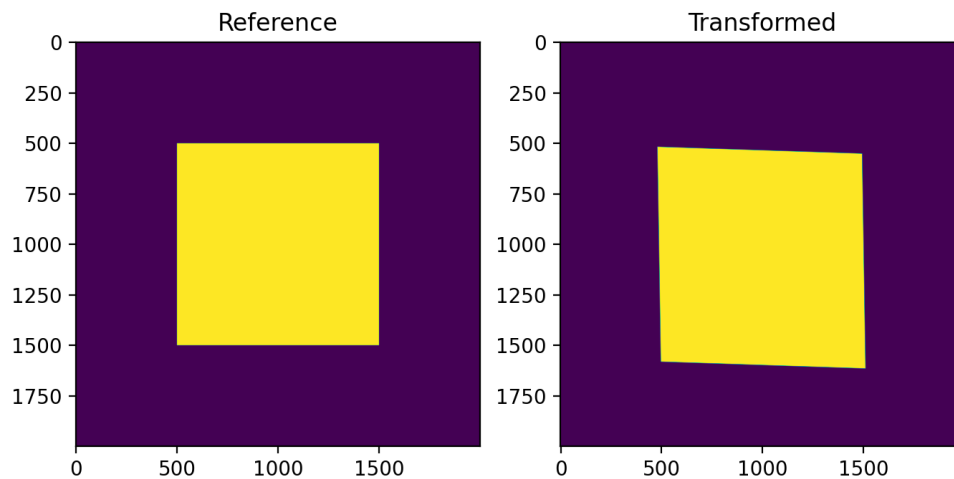


Figure 31 Transformation map obtained via linking HRDIC and EBSD maps

In the next stage, the single grain can be selected to run further analysis. In this example, grain ID 29 is selected. The coloured lines on the grain represent planes normal to the slip direction. The coloured lines are the theoretical tracks for four 111 planes on this grain. The black line gives the measured band from the HRDIC map. The number of bands detected for this grain is one.

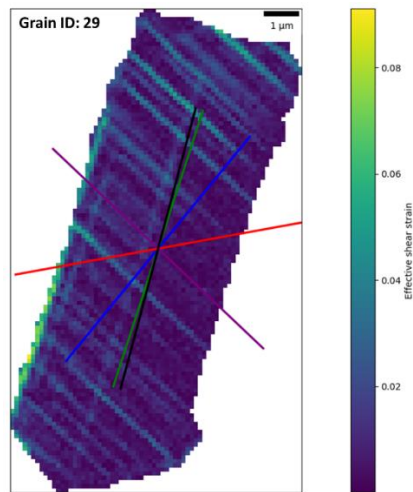


Figure 32 Grain selected for RDR analysis (e.g.: Grain ID 29)

In the RDR analysis, the principle is based on possible Burger vectors associated with slip trace which results in characteristic displacement gradient. From the analysis, a slip band in the grain can be selected to run RDR analysis (Figure 33A). Slip band selection is based on bands with maximum shear strain. From the analysis conducted, the measured RDR value is obtained via the slope of the u-v centred plot and the is 0.994. From the Schmid factor and theoretical calculations, the plane with the higher Schmid factor value is likely to activate slip in the specimen. In-plane (1-11) and direction [-101], the highest Schmid factor value is obtained and is 0.432 and the theoretical RDR value is 0.928 occurring at an average angle of 46.5° .

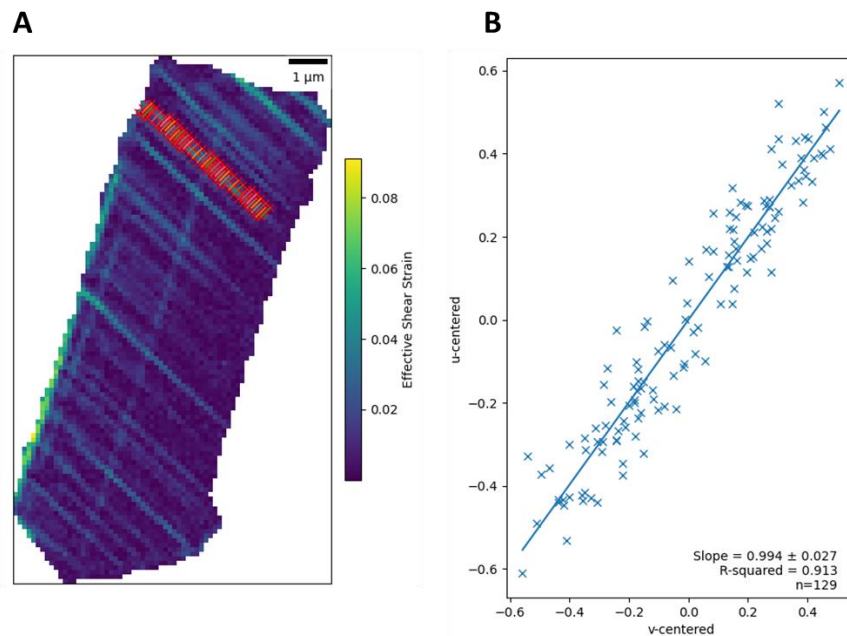


Figure 33 RDR analysis conducted on a single grain (A) selection of slip band for analysis (B) u versus v centred values as the gradient of the linear regression

5 RESULTS AND DISCUSSIONS

5.1 Initial HRDIC and EBSD analysis

The deformation data were obtained from analysis conducted from the surface of a deformed Nickel-based superalloy. The alloys microstructure was controlled for gamma prime precipitates with a diameter of 70nm. To quantify slip bands within single grains, the HRDIC maps are plotted (Figure 34). To measure lattice rotations associated with the slip activity, the EBSD maps are plotted (Figure 35). The data for the analysis was obtained from experiments conducted by Allan Harte et.al. ⁶.

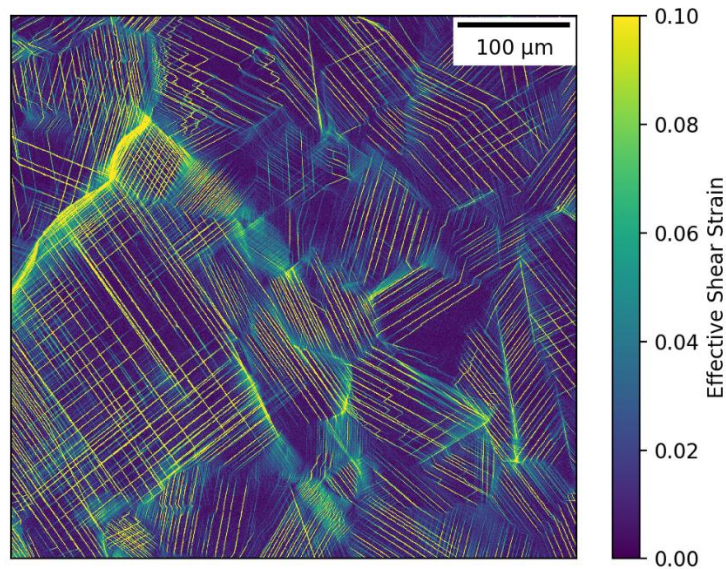


Figure 34 HRDIC map obtained for Ni alloys analysis

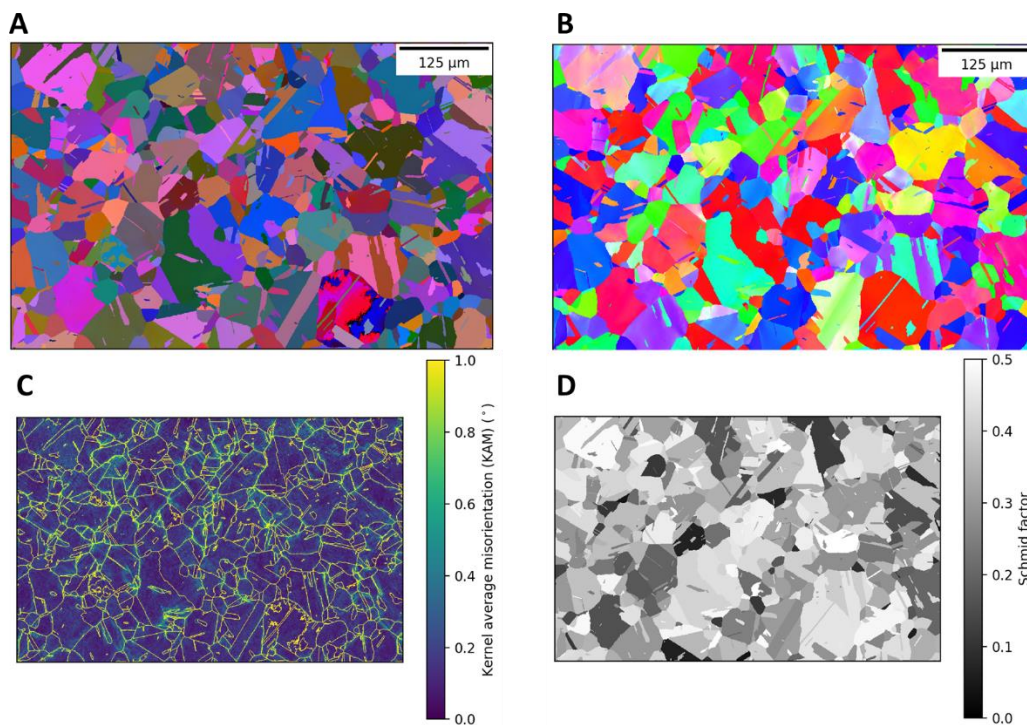


Figure 35 EBSD maps for Ni based superalloys analysis (A) Euler Map (B) IPF Map (C) Kam Map (D) Average Grain Schmid Factors Map

Similarly, a single grain analysis was carried out to obtain the spread, the orientation of the unit cell for the selected grain (Figure 36 A, B). The development of deformation in grains can be attributed by obtaining grain reference orientation deviation map and can track duplex microstructure at several strain levels (Figure 36C).

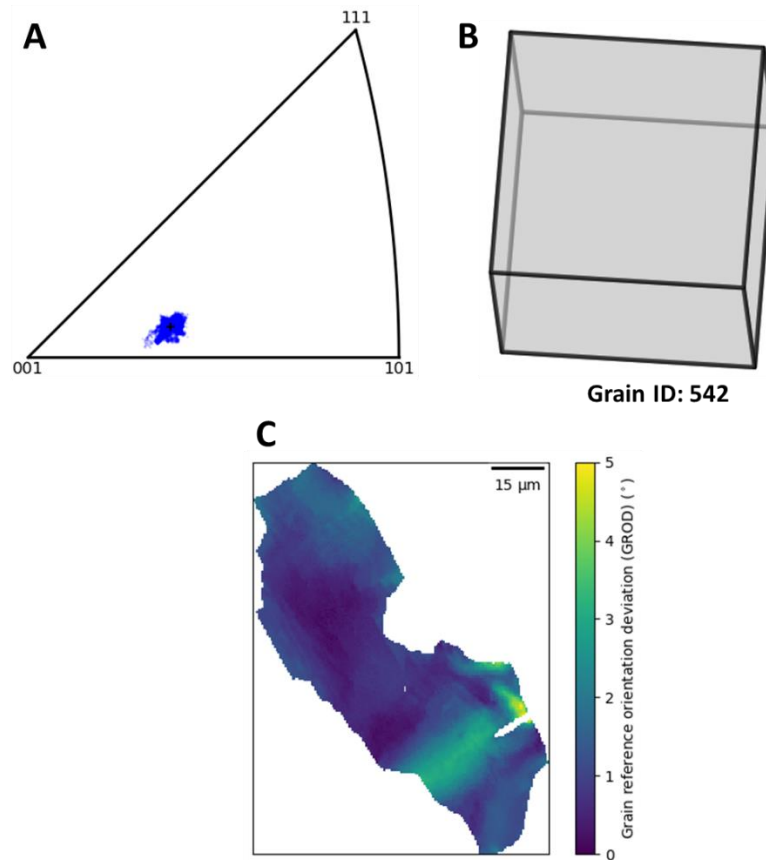


Figure 36 Single grain analysis (A) spread of orientation on an IPF Map (B) Unit Cell (C) GROD, obtained for Grain ID 542

From the single grain analysis obtained, the same can be applied to all the grains and the corresponding spread of orientation can be obtained on an inverse pole figure map (Figure 37A) and the corresponding grain reference orientation deviation map can be obtained for the same (Figure 37B).

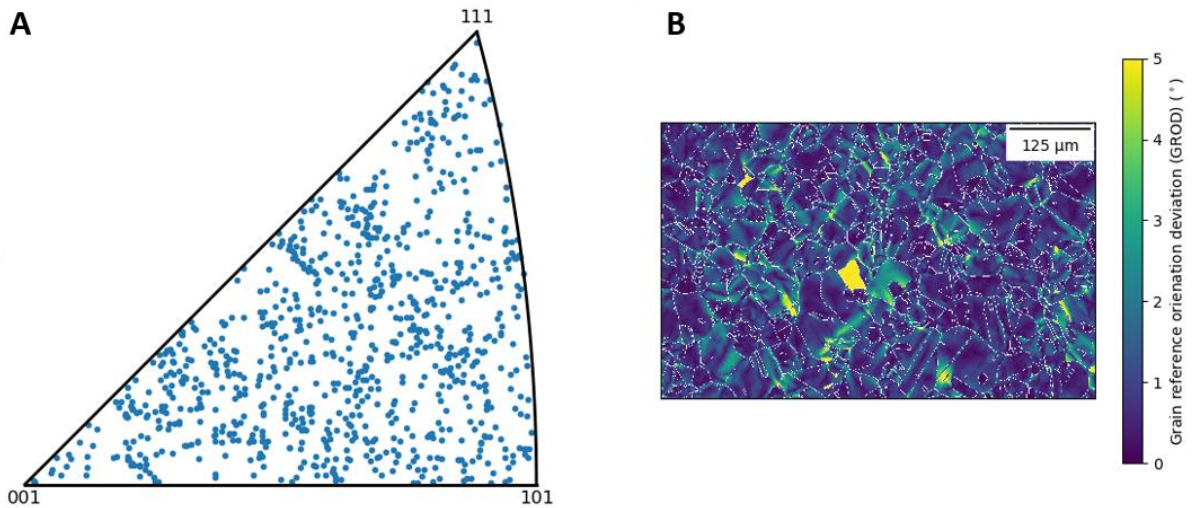


Figure 37 Multigrain analysis (A) Grain orientation in IPF map (B) GROD, obtained for the entire map

5.2 Measurement of slip activity and RDR analysis

To link the HRDIC and the EBSD maps a set of homologous points must be defined. The points must be defined for the DIC map as well as the EBSD map.

Table 4 Homologous points for DIC and EBSD maps

Map	X	Y
DIC	782	110
	1360	330
	53	33
	83	1426
	1306	1264
	711	466
EBSD	179	271
	312	91
	10	36
	19	352
	293	305
	162	125

Once the HRDIC and EBSD maps are linked, further RDR analysis can be carried out to determine the active slip plane in the grain

To identify the active slip in grain, every grain can be selected, and any visible slip band can be selected to run RDR analysis. The measurement of theoretical and measured RDR values was obtained and in conjunction with the Schmid factor value, the active slip planes in the selected grains were identified. Slip bands only

Some grain couldn't be subjected to RDR analysis as the images obtained were out of resolution and blurred to identify the slip bands.

The results from the RDR calculation were obtained and the following results were obtained as in Table 5.

Table 5 Results from RDR calculation for the selected grains

Grain ID	Measured RDR	Theoretical RDR	Max Schmid factor	Angle
6	1.473	1.049	0.473	36.7
7	2.122	2.436	0.495	29
14	0.797	1.047	0.474	37.1
27	1.674	1.134	0.459	41.3
47	1.044	1.747	0.453	34.5
64	1.273	1.837	0.459	34.8
77	1.755	2.686	0.351	66.8
80	2.025	2.281	0.257	59.2

Grain ID 7 has been noted to have a higher Schmid factor value and is likely to be activated in the (1-11) plane and [110] direction.

5.3 Slip variability within a grain

To understand the effects of slip variability within a single grain, multiple slip bands were selected in one single grain and similar RDR analysis was conducted.

In this study grain ID, 7 was selected (Figure 38) and slip bands were selected in different regions within the selected grain boundary as in Figure 39(1-6).

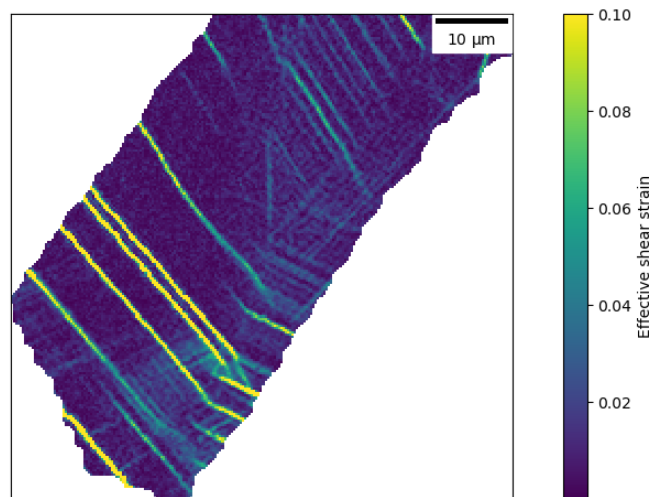


Figure 38 Grain selected for further analysis (Grain ID: 7)

In Figure 39, a total of six slip bands was selected from the grain region. A similar RDR analysis was conducted obtained to compared measured and theoretical calculations via the Schmid factor value. The results of the analysis are as in Table 6.

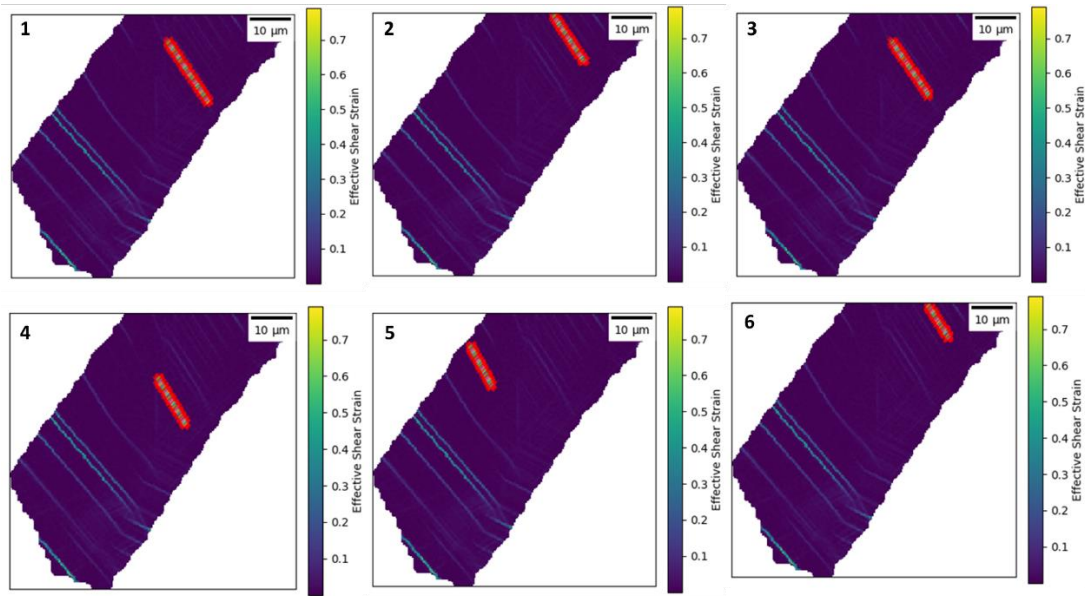


Figure 39 Selection of slip bands to identify variability within a grain

Table 6 Results obtained for slip variability within a grain (for grain ID: 7)

Slip No.	Measured RDR	Theoretical RDR	Max Schmid factor	Angle
1	2.074	2.436	0.495	29
2	0	0.417	0.250	29
3	2.122	2.436	0.495	29
4	0.01	0.417	0.25	29
5	0.399	0.417	0.250	29
6	0.263	0.417	0.250	29

The slips were measured at an angle of 29°. The activation can be observed at different Schmid factor values. The most prominent being observed in Figure 39 1 and 3 (1 & 3 slip no. from Figure 39 and Table 6). In both cases, the activation occurs at (1-11) plane and [110] direction.

6 CONCLUSIONS

A detailed study was conducted in order to study the effects of pre-loading a large specimen up to the plastic strain limit. Due to constraints on accessing the laboratory, experiments couldn't be completed to the fullest. Hence data obtained from previously completed experiments were used in the study to further analyze and provide a complete explanation

A tensile test was conducted on a large specimen and pre-strained to a plastic limit of 12% strain. The pre-strained specimen was then cut in directions 0°, 45°, 90° for carrying in-situ tests. The dimensions of the sample to be prepared is represented in Figure 40.

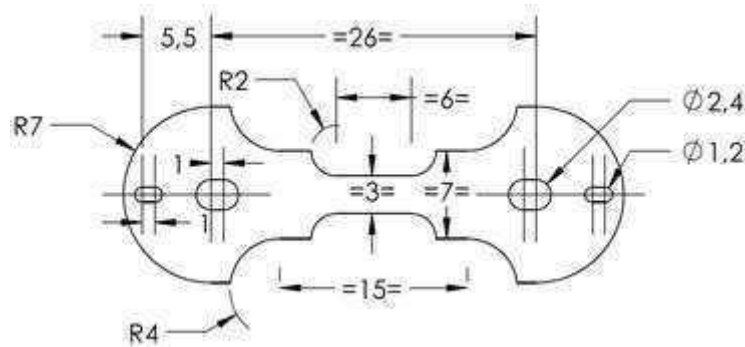


Figure 40 Dimensions of test sample for in-situ test

The sample data obtained for Nickel superalloys were used to conduct further analysis to obtain the corresponding HRDIC and EBSD maps. Homologous points were defined to link the HRDIC and EBSD maps. Further, relative displacement ration analysis was run to obtain u-v centred plot to the RDR value and calculate the Schmid factor. The slip plane with the highest Schmid factor is likely to active slip in the selected grain.

RDR analysis was conducted for different grains and the corresponding results were obtained based on Schmid factor value calculations (Table 5). The results were compared between the theoretical and measured RDR values.

To understand slip variability within the grain, a single grain was selected, and multiple slip bands were selected within the grain region. The prominent slip band was recognized via RDR analysis (Table 6).

7 ACKNOWLEDGEMENTS

The author is grateful for continuous support and guidance from his supervisor, Dr João Quinta da Fonseca. The author is also thankful to Dongchen Hu (PhD student) for help with experiments and analysis. Finally, the author would like to thank his parents for all their love and support during the completion of the course.

8 REFERENCES

- (1) Liu, L.; Zhang, J.; Ai, C. Nickel-Based Superalloys. In *Reference Module in Materials Science and Materials Engineering*; Elsevier, 2020. <https://doi.org/10.1016/B978-0-12-803581-8.12093-4>.
- (2) Maurer, G.; Khalfalla, Y.; Benyounis, K. Y. B. T.-R. M. in M. S. and M. E. Solidification of Superalloys; Elsevier, 2016. <https://doi.org/10.1016/B978-0-12-803581-8.03373-7>.
- (3) Superalloys for Gas Turbine Engines. In *Introduction to Aerospace Materials*; Mouritz, A. P., Ed.; Woodhead Publishing, 2012; pp 251–267. <https://doi.org/10.1533/9780857095152.251>.
- (4) Boeing. 787 Propulsion System https://www.boeing.com/commercial/aeromagazine/articles/2012_q3/2/ (accessed Jul 2, 2021).
- (5) Grzesik, W. Chapter Thirteen - Machinability of Engineering Materials. In *Advanced Machining Processes of Metallic Materials (Second Edition)*; Grzesik, W., Ed.; Elsevier, 2017;

- pp 241–264. <https://doi.org/https://doi.org/10.1016/B978-0-444-63711-6.00013-2>.
- (6) Sperry, R.; Harte, A.; Quinta da Fonseca, J.; Homer, E. R.; Wagoner, R. H.; Fullwood, D. T. Slip Band Characteristics in the Presence of Grain Boundaries in Nickel-Based Superalloy. *Acta Mater.* **2020**, *193*, 229–238. <https://doi.org/https://doi.org/10.1016/j.actamat.2020.04.037>.
 - (7) Harte, A.; Atkinson, M.; Preuss, M.; Quinta da Fonseca, J. A Statistical Study of the Relationship between Plastic Strain and Lattice Misorientation on the Surface of a Deformed Ni-Based Superalloy. *Acta Mater.* **2020**, *195*, 555–570. <https://doi.org/https://doi.org/10.1016/j.actamat.2020.05.029>.
 - (8) ANSYS. CES EduPack Software, Granta Design Limited. ANSYS: Cambridge, UK 2020.
 - (9) Sukumaran, A.; Gupta, R. K.; Anil Kumar, V. Effect of Heat Treatment Parameters on the Microstructure and Properties of Inconel-625 Superalloy. *J. Mater. Eng. Perform.* **2017**, *26* (7), 3048–3057. <https://doi.org/10.1007/s11665-017-2774-8>.
 - (10) Qu, J.; Yang, S.; Chen, Z.; Du, J.; Li, J.; Wang, D. Effect of Turning Amount on Metallurgical Qualities and Mechanical Properties of GH4169 Superalloy. *Materials (Basel)*. **2019**, *12* (11). <https://doi.org/10.3390/ma12111852>.
 - (11) Campbell, F. C. *Phase Diagrams: Understanding the Basics*; ASM International, 2012.
 - (12) Hillier, G.S., Bhadeshia, H. K. D. . The Homogenisation of Single-Crystal Superalloys. In *Proceedings of the Sheffield Centenary Conference on Perspectives in Metallurgical Development, The Metals Society*; London, 1984; pp 183–187.
 - (13) Hillier, G. S.; Rae, C. M. F.; Bhadeshia, H. K. D. H. Extrinsic and Intrinsic Nodes in the Gamma Prime Phase of a Single-Crystal Superalloy. *Acta Metall.* **1988**, *36*, 95–109.
 - (14) Bhadeshia, H. K. D. H. Superalloys <https://www.phase-trans.msm.cam.ac.uk/2003/nickel.html> (accessed Jan 20, 2021).
 - (15) Caceres, P. G. Deformation of Single Crystals. **2014**.
 - (16) Weidner, A.; Beyer, R.; Blochwitz, C.; Holste, C.; Schwab, A.; Tirschler, W. Slip Activity of Persistent Slip Bands in Polycrystalline Nickel. *Mater. Sci. Eng. A* **2006**, *435–436*, 540–546. <https://doi.org/https://doi.org/10.1016/j.msea.2006.07.039>.
 - (17) Madden, P. K.; Harbottle, J. E. The Imaging of Slip Bands in Nickel. *Phys. status solidi* **1978**, *46*, 639–652. <https://doi.org/https://doi.org/10.1002/pssa.2210460229>.
 - (18) Chen, Z.; Daly, S. H. Active Slip System Identification in Polycrystalline Metals by Digital Image Correlation (DIC). *Exp. Mech.* **2017**, *57* (1), 115–127. <https://doi.org/10.1007/s11340-016-0217-3>.
 - (19) Xu, X.; Lunt, D.; Thomas, R.; Babu, R. P.; Harte, A.; Atkinson, M.; da Fonseca, J. Q.; Preuss, M. Identification of Active Slip Mode in a Hexagonal Material by Correlative Scanning Electron Microscopy. *Acta Mater.* **2019**, *175*, 376–393. <https://doi.org/https://doi.org/10.1016/j.actamat.2019.06.024>.
 - (20) Whittaker, M.; Lancaster, R.; Harrison, W.; Pretty, C.; Williams, S. An Empirical Approach to Correlating Thermo-Mechanical Fatigue Behaviour of a Polycrystalline Ni-Base Superalloy. *Materials* . 2013. <https://doi.org/10.3390/ma6115275>.
 - (21) Mankins, W. L. ASM Handbook-Metallography and Microstructures of Nickel and Nickel-Copper Alloys. In *Metallography and Microstructures*; 2004. <https://doi.org/https://doi.org/10.31399/asm.hb.v09.9781627081771>.

- (22) Vander Voort, G.; Manilova, E. Metallographic Techniques for Superalloys. *Microsc. Microanal.* - *MICROSC MICROANAL* **2004**, 10. <https://doi.org/10.1017/S1431927604883442>.
- (23) Norton, R. L. *Machine Design: An Integrated Approach*, 5th ed.; Pearson, 2019.
- (24) ISO. 6892-1:2019(En) Metallic Materials — Tensile Testing — Part 1: Method of Test at Room Temperature. International Organization for Standardization: Geneva, Switzerland 2019.
- (25) E8M-13, A. E. /. Standard Test Methods for Tension Testing of Metallic Materials. ASTM International: West Conshohocken, PA 2013. https://doi.org/10.1520/E0008_E0008M-13.
- (26) INSTRON®. Industrial Series HDX Models <https://www.instron.us/en-us/products/testing-systems/universal-testing-systems/high-force-universal-testing-systems/static-hydraulic/hdx> (accessed Jan 24, 2021).
- (27) Microscopy-Australia. MYSCOPE - Microscopy Training <https://myscope.training/index.html#> (accessed Jan 22, 2021).
- (28) Atkinson, M. D.; Donoghue, J. M.; da Fonseca, J. Q. Measurement of Local Plastic Strain during Uniaxial Reversed Loading of Nickel Alloy 625. *Mater. Charact.* **2020**, 168, 110561. <https://doi.org/https://doi.org/10.1016/j.matchar.2020.110561>.
- (29) Dutkiewicz, J.; Rogal, Ł.; Kalita, D.; Berent, K.; Antoszewski, B.; Danielewski, H.; Węglowski, M. St.; Łazińska, M.; Durejko, T.; Czujko, T. Microstructure and Properties of Inconel 625 Fabricated Using Two Types of Laser Metal Deposition Methods. *Materials (Basel)*. **2020**, 13 (21). <https://doi.org/10.3390/ma13215050>.
- (30) Di Gioacchino, F.; Quinta da Fonseca, J. Plastic Strain Mapping with Sub-Micron Resolution Using Digital Image Correlation. *Exp. Mech.* **2013**, 53 (5), 743–754. <https://doi.org/10.1007/s11340-012-9685-2>.
- (31) LAVISION. Digital Image Correlation (DIC) <https://www.lavision.de/en/techniques/dic-dvc/> (accessed Feb 9, 2021).
- (32) Atkinson, Michael D, Thomas, Rhys, Harte, Allan, Crowther, Peter, & Quinta da Fonseca, J. DefDAP: Deformation Data Analysis in Python (Version 0.92). Zenodo. <https://github.com/MechMicroMan/DefDAP>.
- (33) Nolze, G.; Hielscher, R. IPF Coloring of Crystal Orientation Data. *J. Appl. Crystallogr.* **2015**, 1–17.
- (34) Gutierrez-Urrutia, I.; Archie, F.; Raabe, D.; Yan, F.-K.; Tao, N.-R.; Lu, K. Plastic Accommodation at Homophase Interfaces between Nanotwinned and Recrystallized Grains in an Austenitic Duplex-Microstructured Steel. *Sci. Technol. Adv. Mater.* **2016**, 17 (1), 29–36. <https://doi.org/10.1080/14686996.2016.1140302>.